



Reducing the high hydrogen binding strength of vanadium carbide MXene with atomic Pt confinement for high activity toward HER

Seungyoung Park^{a,1}, Yea-Lee Lee^{b,1}, Yeoheung Yoon^a, Se Yeon Park^a, Soonmin Yim^a,
Wooseok Song^a, Sung Myung^a, Kug-Seung Lee^c, Hyunju Chang^b, Sun Sook Lee^{a,*},
Ki-Seok An^{a,*}

^a Thin Film Materials Research Center, Korea Research Institute of Chemical Technology, Yuseong, Daejeon 34114, Republic of Korea

^b Chemical Data-driven Research Center, Korea Research Institute of Chemical Technology, Yuseong, Daejeon 34114, Republic of Korea

^c Pohang Accelerator Laboratory, 80 Jigokro-127-beongil, Nam-gu, Pohang Gyeongbuk 37673, Republic of Korea.

ARTICLE INFO

Keywords:

V₂CT_x MXene

Pt single atom

Hydrogen evolution reaction

Active sites

ABSTRACT

To construct an efficient electrocatalyst for HER, the high binding energy of MXene must be mitigated through electronic modulation of active sites. Here, we propose atomic Pt substitution in V₂CT_x MXene to modulate the electronic structure and promote catalytic activity toward HER. Pt–V₂CT_x exhibits high HER performance with a low overpotential of 27 mV at –10 mA cm^{–2} in acidic media, comparable to the commercial Pt/C catalyst. X-ray absorption spectroscopy and DFT calculations indicate that the Pt atoms are efficiently confined to the V vacancy sites of V₂CT_x, accompanied by a unique electronic structure. The atomic substitution of Pt with higher occupied d states at the Fermi energy of Pt and surface oxygen sites can significantly indicate an optimum hydrogen-binding free energy (ΔG_{H^*}), promoting HER performance. This work introduces further prospects for developing efficient electrocatalysts by feasible electronic regulation and highly improved catalytic activity through rational atomic engineering.

1. Introduction

Electrocatalytic water splitting is a powerful technology that generates clean hydrogen without emitting greenhouse gases, enabling the mass production of hydrogen via a renewable energy route [1,2]. Highly active electrocatalysts with low overpotentials are necessary for the fast kinetics of HER [3]. To date, Pt and other precious metals have been used as highly efficient electrochemical catalysts. However, owing to the low reserves, high price, and scarcity of noble metal catalysts, their use is limited to industrial applications only [4]. Thus, it is crucial to find inexpensive alternatives, having abundant reserves, while exhibiting excellent catalyst efficiency [5]. For the past several years, various two-dimensional (2D) material-based materials have been studied as substitutes for precious metal catalysts. Transition metal-based compounds, including dichalcogenides, phosphides, nitrides, and carbides, have attracted considerable attention as promising heterogeneous catalysts [6–11]. Particularly, MoS₂, which has an electronic structure similar to that of Pt, has attracted considerable attention, owing to its

favorable HER performance. However, although MoS₂ is the most prominent alternative HER catalyst, it remains far from practical applications and requires specific interventions, such as activation of the inactive in-plane surface, maximizing active edge sites, and metallic conduction, which emerges in the thermodynamically unstable 1T-phase of MoS₂ [6,12].

MXene, a new family of emerging 2D layered materials consisting of transition metal carbides, nitrides, and carbonitrides, has attracted significant attention in energy storage and conversion, electromagnetic, and electronic applications [13–15]. Furthermore, MXene can be a potential HER electrocatalyst, having intrinsic metallic characteristics with surface terminal groups and vacancy sites generated during the synthetic process [16,17]. However, pristine MXene materials, except for Mo-based MXene, exhibit poor catalytic performance [18]. Nevertheless, adequate HER catalytic performance can be achieved through the chemical and structural modifications of MXenes, including oxygen-functionalized Ti₃C₂T_x, nitrogen-modified-Ti₃C₂T_x, and Pt-Mo₂TiC₂T_x, using variable surface functional groups and surface

* Corresponding authors.

E-mail addresses: sunsukl@kriict.re.kr (S.S. Lee), ksan@kriict.re.kr (K.-S. An).

¹ These authors contributed equally to this work

defects [19–21]. With the expectation from the same series as Mo, MXenes based on group VB metals, including Nb or V, are also regarded as promising HER catalysts. V-based materials with versatile structural and oxidation states can be tailored for electronic structure, conductivity, and ion diffusion. In addition, catalytic properties, including the activity of metallic sites, can be tuned when integrated with other materials [22]. Notably, vanadium carbide exhibits comparable hydrogen adsorption properties in comparison to Mo or Nb-based carbides [23]. In addition, recent studies on V-based electrocatalysts for water splitting (HER and oxygen evolution reaction (OER)) have been reported [22,24]. In particular, V-based or V-doped materials for OER have gained significant attention owing to their enhanced conductivity and decreased charge-transfer resistance, which is favorable for improved catalytic activity [22,24]. Therefore, V is expected to be an excellent candidate for HER electrocatalysts. However, when V_2CT_x is used as an HER catalyst, the hydrogen adsorption is too strong and shows an inferior catalytic performance [25].

According to a previous simulation work with a fully oxygen-terminated surface (V_2CO_2) for evaluating HER performance, the thermodynamically stable V_2CO_2 showed a high reaction free energy of hydrogen adsorption, theoretically revealing the unsuitable HER catalytic activity [25]. However, even in the case of transition metal-adsorbed V_2CO_2 , the adsorption energy for hydrogen is moderate, leading to less charge transfer from H to O and weakening the interaction between H and O. In addition, the P-doping process in V_2CT_x MXene weakened the H-O bonding and enhanced the catalytic activity toward HER, controlling the bonding of P atoms in V_2CT_x . Through the doping process of P atoms, $P-V_2CT_x$ could not achieve sufficient HER activity [26]. Thus, for a remarkable HER electrocatalyst with V_2CT_x , an appropriate modification process of MXene is necessary to achieve the proper hydrogen adsorption strength for accelerating the HER performance. Thus, Pt atoms can be an excellent option for confinement in V_2CT_x nanosheets. The atomic confinement of Pt can maximize its HER efficiency with high intrinsic catalytic properties through doping of vacancy sites in V_2CT_x . The reactive and reductive V_2CT_x MXene can provide adequate sites for confinement of Pt atoms, which can be substituted for the V vacancy sites. Furthermore, the electron transfer from Pt to the matrix material (V_2CT_x nanosheet) is beneficial for promoting the HER performance of V_2CT_x nanosheets and weaken the H-O strength because of the extra charge from the metallic electron donors. This presents the possibility of excellent catalytic performance [27–29]. Thus, Pt atom-confined V_2CT_x has the potential for high HER performance by maximizing the utilization efficiency of Pt atoms and offer optimal adsorption energy for hydrogen.

Herein, we report the first atomically Pt-immobilized V-based MXene (V_2CT_x) nanosheets via a simultaneous self-reduction process of Pt into V-rich defect sites based on the highly reductive nature of V_2CT_x . During Al etching and delamination of single- or few-layered MXene nanosheets, HF can generate adjacent V vacancies even under mild conditions. V vacancies, which are very unstable and reactive in highly reductive MXene nanosheets, can accommodate and immobilize Pt atomically. Pt atoms are confined to the V vacancies of V_2CT_x with a low loading amount (~ 0.88 wt%), and covalent Pt–C bonds are formed with the surrounding carbon atoms. The resultant Pt– V_2CT_x catalysts exhibited Pt-like kinetics toward the HER, delivered highly enhanced catalytic activity with a low overpotential of ~ 27 mV at 10 mA cm^{-2} in $0.5\text{ M H}_2\text{SO}_4$, and showed excellent stability. Notably, the Pt– V_2CT_x catalyst demonstrated a 50.1-fold increase in activity compared to the state-of-the-art commercial Pt/C catalyst. Even in an alkaline electrolyte (1 M KOH), the Pt– V_2CT_x catalyst exhibited excellent catalytic activity with an overpotential of ~ 68 mV, demonstrating HER performance over an alkaline media. Extended X-ray absorption fine spectroscopy (EXAFS) suggested the presence of positively charged Pt atoms, indicating atomic lattice confinement in V_2CT_x . DFT calculations show that single Pt atoms confined to V vacancies and surface oxygen atoms of V_2CT_x nanosheets act as efficient active sites, indicating the optimal Gibbs free energy for

adsorption of atomic hydrogen (ΔG_H^0), resulting in outstanding HER performance.

2. Material and methods

2.1. Synthesis of V_2CT_x & Pt- V_2CT_x MXene nanosheet

Al layer of V_2CT_x MXene was selectively etched by HF solution (49%) at 35°C for 5 days, and neutralized by the D.I washing using centrifuge. And then, as-prepared V_2CT_x MXene was dispersed in TBAOH (Tetrabutylammonium hydroxide) solution and stirred for 24 h for the intercalation of TBAOH into V_2CT_x MXene. After the stirring, the TBAOH intercalated V_2CT_x MXene was neutralized with the D.I washing and then, shaken for 20 min for delaminated V_2CT_x MXene nanosheets. The delaminated V_2CT_x solution was then centrifuged at 3000 rpm to remove the un-delaminated V_2CT_x MXene sheets. Pt- V_2CT_x MXene nanosheet was prepared by self-reduction process using H_2PtCl_6 solution. The desirable amount (100 μL , 200 μL , 500 μL) of H_2PtCl_6 (10 mg/ml) was added into V_2CT_x solution and then, the homogeneous solution was stirred at room temperature for 6 h for self-reduction of Pt atom into V_2CT_x to provide the Pt- V_2CT_x without heat treatment. After the reaction, the Pt- V_2CT_x solution was filtrated and washed with D.I water and ethanol to remove the excess H_2PtCl_6 .

2.2. Material characteristics

The morphological study of the sample was characterized by field-emission scanning electron microscopy (FE-SEM, S-4700, Hitachi). Transmission electron microscopy (TEM), Energy-dispersive X-ray spectroscopy (EDS) and high-angle annular dark-field scanning transmission electron microscopy (HAADF-STEM) were performed using a JEOL ARM200F with a field-emission gun operated at 200 kV and an aberration corrector. X-ray diffraction analysis (XRD, Rigaku) was conducted to identify the crystal phases of the products with $\text{Cu K}\alpha$ radiation ($\lambda = 1.5418\text{ \AA}$) at the current of 40 mA and the voltage of 40 kV. The chemical bonding was examined by Raman spectroscopy (inVia Raman spectroscopy, Renishaw) and X-ray photoelectron spectroscopy (XPS, K-alpha, ThermoFinnigan) with monochromatic Al $\text{K}\alpha$ radiation. X-ray absorption fine structure (XAFS) was measured at 8 C nano-probe XAFS beamline (BL8C) of Pohang Light Source (PLS-II) in the 3.0 GeV storage ring, with a ring current of 250 mA. The X-ray beam was monochromated by a Si(111) double crystal where the beam intensity was reduced by 30% to eliminate the higher-order harmonics. The x-ray beam was then delivered to a secondary source aperture where the beam size was adjusted to be $0.5\text{ mm (v)} \times 1\text{ mm (h)}$. XAFS spectra were collected in fluorescence mode. The obtained spectra were processed using Demeter software. Extended x-ray absorption fine structure (EXAFS) spectra were fitted in a Fourier-transform range of $3\text{--}10\text{ \AA}^{-1}$ with a Hanning window applied between 1.0 \AA and 3.0 \AA . The amplitude reduction factor (S_0^2) was set to be 0.8. The Pt content was detected by Inductively coupled plasma atomic emission spectroscopy (ICP-AES).

2.3. Electrochemical characterization

The loading of catalysts (V_2CT_x , Pt- V_2CT_x and 20% Pt/C) on the working electrode was prepared with general method for the catalyst ink. First, 10 mg of catalyst was dispersed in aqueous ethanol (0.9 ml of D.I water and 0.1 ml Ethanol) with 50 μL of 5 wt% Nafion ethanol solution. Then, 20 μL of catalyst ink was drop-coated on 4 mm glassy carbon electrode with catalyst loading of 1.59 mg cm^{-2} . All electrochemical measurements were conducted with a typical three-electrode cell using a potentiostat (MP1, Wonatech), where the glassy carbon with 4 mm diameter as the working electrode (WE), a graphite rod was used as the counter electrode (CE). Ag/AgCl electrode and Hg/HgO were used as the reference electrode (RE) for acidic electrolyte and alkaline

electrolyte, respectively. 0.5 M H_2SO_4 and 1 M KOH were used as electrolyte for acidic and alkaline electrolyte, respectively. LSV curves were characterized from 0.00 to -0.80 V vs RHE at a scan rate of 10 mV s^{-1} . The stability was tested by galvanostatic measurement for the voltage–time response at a static potential of -10 mA cm^{-2} vs RHE for up to 10 h. Potentials reported in this work were referenced to a RHE according to the following equation:

For Ag/AgCl electrode, $E(\text{RHE}) = E_{\text{Ag/AgCl}} + 0.197 + 0.0591 \text{ pH}$.

For Hg/HgO electrode, $E(\text{RHE}) = E_{\text{Hg/HgO}} + 0.098 + 0.0591 \text{ pH}$.

2.4. Theoretical computation

We have performed density functional theory (DFT) calculations using the projector augmented wave (PAW) method as implemented in the Vienna Ab Initio Simulation Package (VASP) [30,31]. The exchange-correlation interactions were described by the generalized gradient approximations (GGA) in the form of the Perdew-Burke-Ernzerhof functional. The van der Waals interaction was described by using the Tkatchenko-Scheffler method [32]. The cutoff energy was set to 600 eV, and the convergence tolerance for the residual force on each atom during structure relaxation were set to 0.005 eV/Å. The vacuum space in the z-direction was $> 13 \text{ Å}$, which was enough to

prevent the interaction between periodical images. The Brillouin zone was sampled with the Monkhorst-Pack mesh with a K-point of $3 \times 3 \times 1$ and $20 \times 20 \times 1$ for the $4 \times 4 \times 1$ supercell during structural optimization and density of states calculation, respectively. The Gibbs free energy of the adsorption of the intermediate hydrogen on a catalyst (ΔG_{H^*}) is obtained by $\Delta G_{\text{H}^*} = \Delta E_{\text{B}} + \Delta E_{\text{ZPE}} - T\Delta S_{\text{H}} = \Delta E_{\text{B}} + 0.24$, where ΔE_{B} is the binding energy of atomic hydrogen, and ΔE_{ZPE} and ΔS_{H} are the difference in zero-point energy and the entropy between the atomic hydrogen adsorbed state and hydrogen in the gas phase, respectively.

3. Results and discussion

3.1. Synthesis and structural characteristic of Pt- V_2CT_x

Fig. 1a presents the overall process for the synthesis of delaminated V_2CT_x and Pt- V_2CT_x nanosheets. Multilayer-structured V_2AlC MAX was selectively etched using HF solution to remove the Al layer, providing V_2CT_x MXene with spontaneously generated terminal groups ($\text{T}_x = -\text{F}, -\text{O}, -\text{OH}$). The layered structure of V_2CT_x with the cavity caused by the etched Al layer was distinctly observed (Fig. 1b). Furthermore, to synthesize thin V_2CT_x nanosheets, layered V_2CT_x was intercalated with

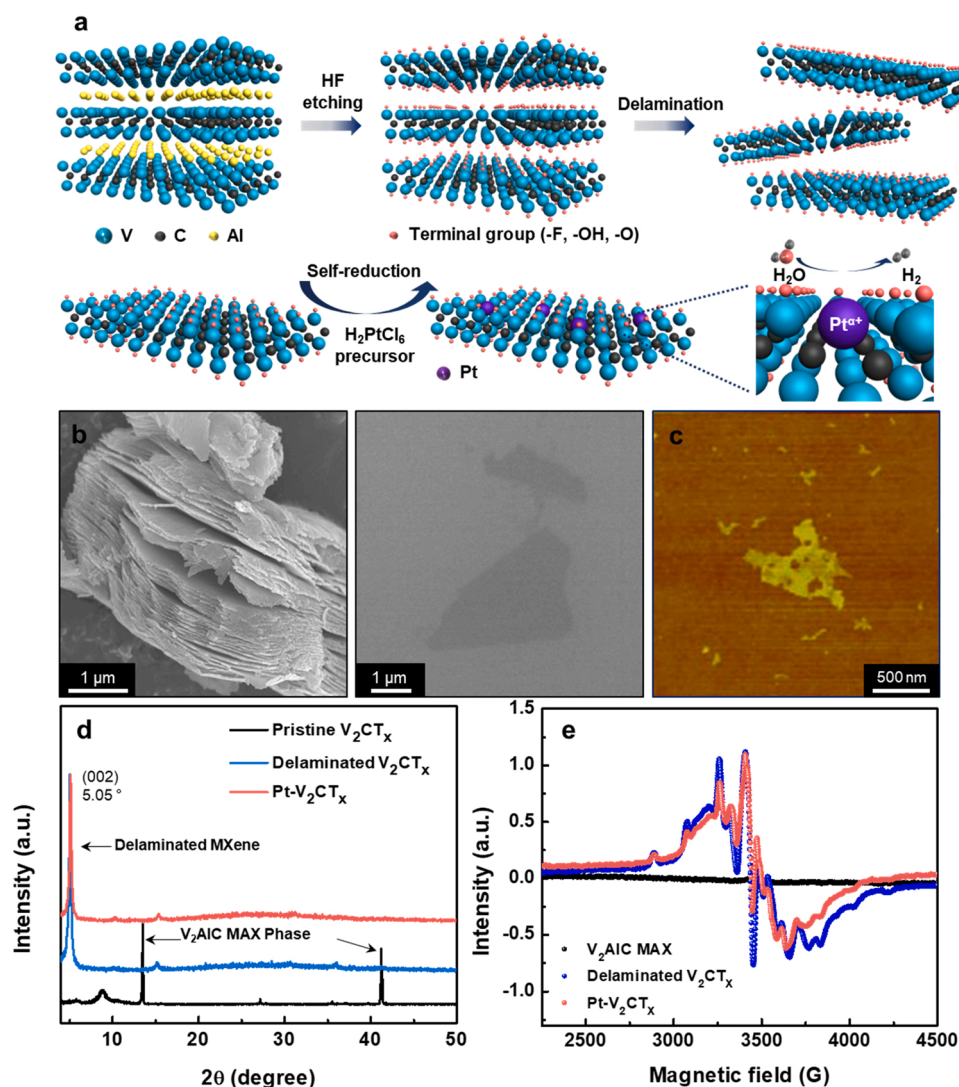


Fig. 1. Structural characteristics of Pt- V_2CT_x nanosheets. (a) Schematic illustration for synthesis of Pt- V_2CT_x nanosheets. (b) SEM images of V_2CT_x nanosheets, (c) AFM image of Pt- V_2CT_x nanosheet. (d) XRD patterns of pristine V_2CT_x , delaminated V_2CT_x and Pt- V_2CT_x nanosheets. (e) Electron paramagnetic resonance of V_2AlC MAX, delaminated V_2CT_x , and Pt- V_2CT_x nanosheets.

TBAOH solution and then delaminated (Fig. S1). V–Al bonds were broken during the selective Al etching process, forming V atom vacancies in V_2CT_x . These V vacancies, which were formed naturally during synthesis, were highly unstable and reductive, acting as active sites to confine the Pt atoms. When the H_2PtCl_6 precursor solution is added to the V_2CT_x solution, $[PtCl_6]^{2-}$ ions are uniformly adsorbed and slowly reduced by the unstable and reductive V vacancies on the V_2CT_x surface, inducing the stable doping of atomic Pt to form Pt– V_2CT_x . This process is a spontaneous reaction in which the reduction of Pt atoms proceeds simultaneously with the adsorption of Pt ions [33]. To support the self-reduction of Pt atom, we estimated that the possibility of single atom immobilization in the vacancy site considering the zeta potential and DFT simulation results (Fig. S2 and S3). The zeta potential indicated the negative surface charge of -19.74 mV. This causes a repulsive force with $[PtCl_6]^{2-}$, by the surface negative charge of MXene, and is expected to prefer immobilization by being substituted for an unstable vacancy site rather than being adsorbed and aggregated on the surface of MXene. To supplement this suggestion energetically, we conducted the DFT calculation for the binding energy of the Pt atom in both case which are the surface terminated O site and V metal vacancy site. Comparing the binding energy of Pt attachment to the surface terminated O site and the attachment to the V metal vacancy site, when the Pt atom was substituted for the V vacancy and immobilized (-5.813 eV), it was found to be much more energetically stable than that of the terminated O site (-2.404 eV). Also the optimum binding energy (-5.813 eV) of the Pt atom in the V metal vacancy site is comparable to the cohesive energy of the Pt atom (5.84 eV/atom) indicating the stable nature of Pt atom in V vacancy of V_2CT_x . Based on these results, substitution and immobilization of the V vacancy site of V_2CT_x MXene is considered to be a favorable reaction. The surface characteristics of the as-synthesized Pt– V_2CT_x were analyzed using atomic force microscopy (AFM). The AFM images (Fig. 1c and Fig. S4) indicate that the as-synthesized Pt– V_2CT_x showed a single layer thickness (< 2 nm), suggesting a smooth surface without any change in the Pt– V_2CT_x surface, which may be caused by other rough reduction processes. Additionally, the X-ray diffraction (XRD) pattern demonstrated the delaminated structure and isolated Pt atoms on the Pt– V_2CT_x . Fig. 1d illustrates the XRD patterns of V_2CT_x after delamination and the Pt doping process, indicating the structural change of V_2CT_x . Layered V_2CT_x after HF treatment for Al etching showed a 002 peak at a two theta of 8.86° . This peak can be assigned to a c-lattice parameter (c-LP) of 19.9 Å, which is a characteristic of the typical HF-treated V_2CT_x [34]. After TBAOH treatment, a significant change in the XRD pattern is observed with the downshift of the 002 peak from two theta of 8.86° (c-LP = 19.9 Å) to 5.05° (c-LP = 34.9 Å), indicating an increase in the interlayer distance and delamination of V_2CT_x . Furthermore, the XRD pattern of Pt-substituted V_2CT_x shows only the characteristic peaks of V_2CT_x MXene. The peaks corresponding to Pt NPs and distinct peak changes of V_2CT_x were not observed, indicating that the introduction of Pt atoms did not significantly alter the V_2CT_x structure.

In addition, we conducted electron paramagnetic resonance (EPR) analysis to reveal that the Pt atom is atomically substituted for V vacancies (Fig. 1e). The EPR spectrum of delaminated V_2CT_x MXene confirmed a G-factor of 2.006 at the sharp peak in the middle of the graph using the resonance equation. In addition to the prominent sharp peak at $G = 2.006$, the surrounding peaks, formed owing to the hyperfine structure, are generated by the nuclear and electron spin interactions of V and are likely caused by V-based bonds formed from V_2CT_x with variable terminal groups. The G-factor of 2.00 is typically caused by defects or radicals formed by an atomic vacancy in the structure. Therefore, the EPR peaks confirm the V vacancies generated during the V_2CT_x MXene synthesis. However, in the case of V_2AlC MAX, no distinct EPR peaks were observed [35]. Furthermore, in the case of Pt– V_2CT_x , the intensity at the G-factor of 2.006 was distinctly reduced, implying the reduction of existing V vacancies. The number of V vacancy sites decreased owing to substitution by Pt atoms, and Pt was adsorbed and reduced at the naturally formed V vacancies of V_2CT_x MXene.

3.2. Demonstration for atomic Pt confinement of Pt– V_2CT_x

To verify the distribution and configuration of Pt atoms on V_2CT_x , transmission electron microscopy (TEM) and scanning transmission electron microscopy (STEM) analyses were conducted. Typical TEM images show that the as-synthesized Pt– V_2CT_x nanosheet displayed precise surface morphologies without the presence of any aggregated Pt nanoparticles (Fig. 2a and Fig. S5). The atomic-resolution high-angle annular dark-field scanning transmission electron microscopy (HAADF-STEM) images of the Pt– V_2CT_x nanosheet revealed uniformly distributed small bright dots indicating Pt atoms (Fig. 2b). Atomic sites containing Pt show higher contrast than the adjacent V–C bonds because Pt has a larger atomic number, demonstrating the presence of single Pt atoms on V_2CT_x nanosheets. Moreover, Fig. 2c shows that the bright dots of Pt atoms were located at the lattice of the V plane, indicating that the single Pt atoms were stabilized at the V vacancies by substitution rather than interstitial doping. The selected area electron diffraction (SAED; inset in Fig. 2c) patterns revealed the hexagonal structure of V_2AlC , as previously reported [26]. Fig. 2d displays the intensity profiles of lines A and B in Fig. 2b, indicating that the Pt atoms were stabilized at the V vacancies. The line profiles show the interatomic distances and different intensities of the bright atoms, indicating isolated Pt atoms. Moreover, STEM images and corresponding energy-dispersive X-ray (EDX) spectroscopy elemental analysis demonstrated the distribution of Pt throughout the Pt– V_2CT_x surface, confirming that Pt atoms are uniformly dispersed on the V_2CT_x nanosheets (Fig. 2e).

To further investigate the atomic substitution of Pt atoms in V_2CT_x , we conducted X-ray photoelectron spectroscopy (XPS) and X-ray absorption spectroscopy (XAS). High-resolution XPS spectra of V 2p for pristine V_2CT_x show different peaks in the range of 513–526 eV (Fig. 3a). The lower energy peak of 513 eV is assigned to the V–C bond, and the additional peaks of V-based oxidative species, V^{2+} to V^{5+} , are located at a broad higher energy level. Notably, these peaks in pristine V_2CT_x show a similar trend in the energy levels with the reported results for V_2CT_x and correspond to the defects and V interactions with terminal atoms caused by Al etching after HF treatment [36]. Furthermore, the Raman spectra showed the typical peaks of V_2CT_x (Fig. S6). In comparison to pristine V_2CT_x , Pt– V_2CT_x showed slightly oxidative V 2p spectra, indicating the oxidation state of V, which is slightly higher owing to the introduction of Pt atoms. Fig. 3b shows the high-resolution C 1s spectra. The two peaks at 282.0 and 284.6 eV correspond to the C–V and C–C bonds in pristine V_2CT_x , respectively. The Pt– V_2CT_x spectra showed that the C–C peak was slightly shifted to lower energy. In addition, a weak peak emerged, which is derived from the partial bonding of C to Pt and V. In the Pt 4f spectra, Pt– V_2CT_x exhibited dominant peaks at 71.9 and 75 eV for Pt 4f_{7/2} and Pt 4f_{5/2}, respectively (Fig. 3c). These Pt peaks indicate the positively charged state of Pt atoms in comparison to Pt/C, which displayed peaks at 71.1 eV and 74.3 eV corresponding to metallic Pt. These XPS results demonstrate that the Pt atoms are partially bonded to V_2CT_x , indicating the introduction of Pt–C, consistent with the C 1s spectra of Pt– V_2CT_x . Furthermore, the Pt L3-edge extended X-ray absorption fine structure (EXAFS) oscillations of Pt– V_2CT_x demonstrated the only prominent shell located at 1.6 Å (Fig. 3d, Fig. S7 and Table S1). We compared reference samples of PtO₂ and Pt foil to confirm the Pt state and observed that the Pt–Pt contribution at approximately 2.7 Å found in Pt foil is absent in Pt– V_2CT_x , thereby indicating that there are no Pt particles in Pt– V_2CT_x . Instead, the prominent shell located at 1.6 Å primarily corresponds to Pt–C bonds. Furthermore, the EXAFS fitting results and parameters clearly show the bonding nature of the Pt atom. The fit provides the Pt–C coordination number of 3 for Pt– V_2CT_x , meaning that the single atom site Pt in the Pt– V_2CT_x nanosheet is bound to three C atom. These results indicate that each Pt element is immobilized in V vacancy and forms three stable Pt–C bonds with the surrounding C element. In addition, when immobilized at the vacancy site, it bonds with the surrounding O-terminated atoms on the remaining V atoms, providing the Pt–O coordination number of 2

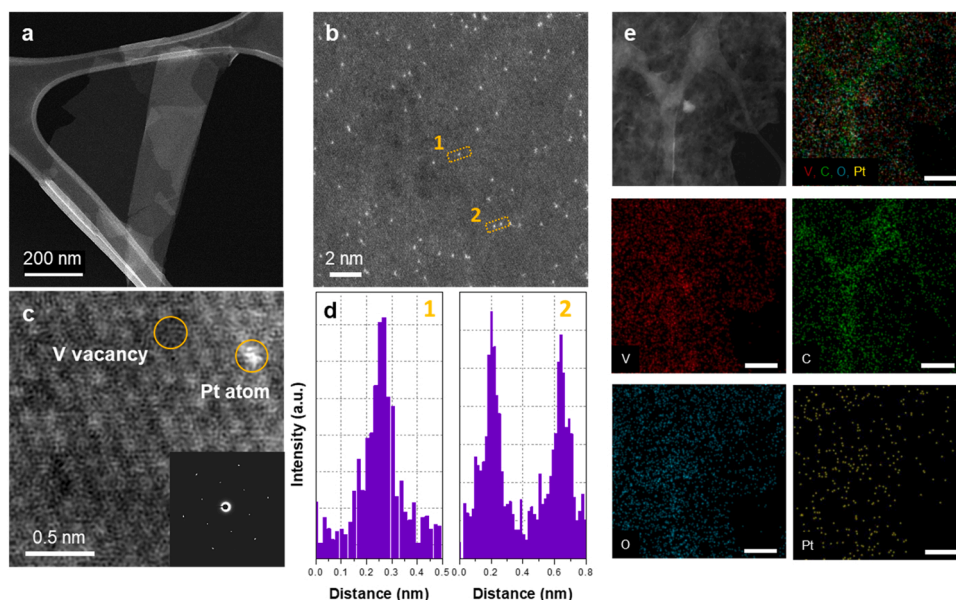


Fig. 2. Morphological characterization of Pt-V₂CT_x nanosheets. (a) STEM images of low-magnification of TEM image of Pt-V₂CT_x nanosheet. (b) high-magnification of STEM image of Pt-V₂CT_x nanosheet. (c) HADDF-STEM images of Pt-V₂CT_x nanosheet. (d) Corresponding line-scanning intensity profile in rectangular region 1 and 2 in b. (e) TEM-EDS mapping image of Pt-V₂CT_x nanosheets.

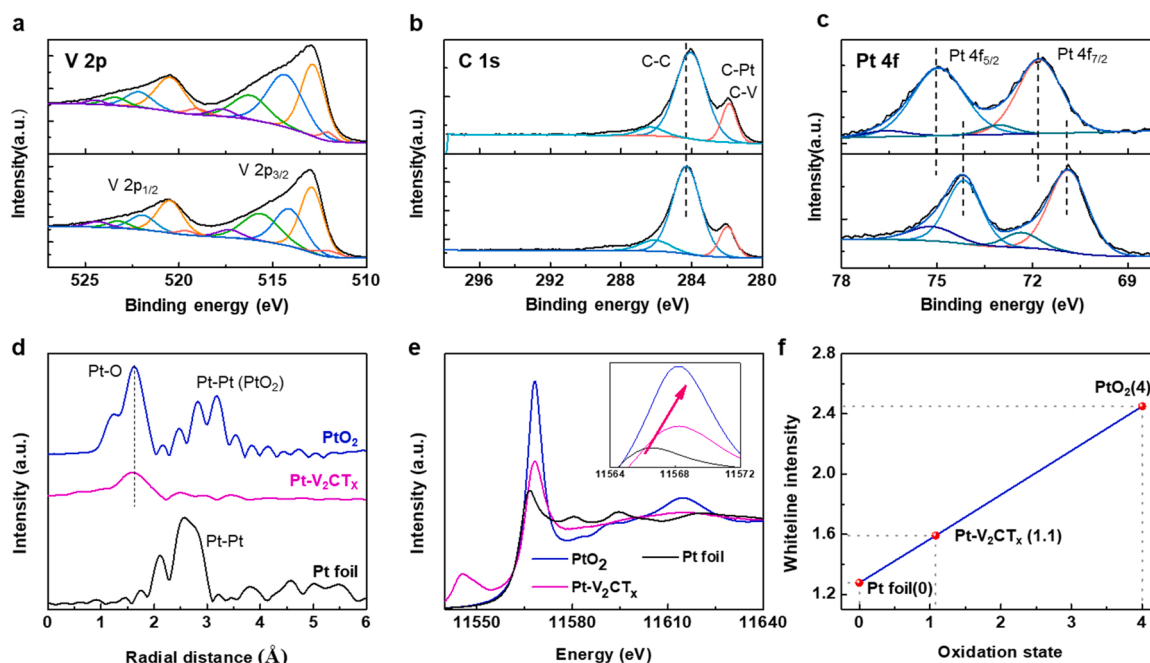


Fig. 3. Electronic structure of Pt-V₂CT_x nanosheets with X-ray photoelectron spectroscopy (XPS) and X-ray absorption spectroscopy (XAS). (a) V2p spectra and (b) C 1s spectra of pristine V₂CT_x in bottom and Pt-V₂CT_x in top. (c) Pt 4f spectra of Pt/C (20%) in bottom and Pt-V₂CT_x in top. (d) k²-weighted FT spectra from EXAFS and (e) normalized XANES spectra at the Pt L3 edge of Pt-V₂CT_x, PtO₂, and Pt foil. (f) The average oxidation state derived from normalized XANES spectra.

which is identical as predicted by modeling of DFT simulations. Based on these results, the Pt atom is not directly adsorbed to the O-terminated atom present on the surface of V₂CT_x nanosheet, but is immobilized at the V vacancy site forming the 3 Pt-C bonds and 2 Pt-O bonds with surrounding C atom and surrounding O-terminated atom. Thus, both the single Pt atom immobilization with V vacancy and O-terminal groups of MXene should play an important role in stable Pt atom immobilization. L₃-edge X-ray absorption near-edge structure (XANES) spectra were used to evaluate the electronic structure of the Pt species (Fig. 3e and f). The L₃ absorption edge of Pt is associated with the transition from the 2p

core levels to the empty states, which is the white line related to the unoccupied d-states of Pt. The white line intensity of Pt-V₂CT_x, which signified the unoccupied d-states of Pt, was higher than that of the Pt foil. This confirmed the positive valence state (1.1) of Pt atoms, which corresponded to the electron transfer from Pt to V₂CT_x in Pt-V₂CT_x in Fig. 3f. Notably, a pre-edge at 11,547 eV is observed for Pt-V₂CT_x, which can be attributed to the orbital hybridization between the 4f and 5d orbitals during Pt immobilization, corresponding to the Pt-mesoporous carbon matrix, indicating Pt-C bonding [37]. These results suggest that atomic Pt was strongly coupled with the V₂CT_x nanosheets, indicating the

formation of Pt–C bonds, which is consistent with the XPS results. Therefore, the above results confirm that single Pt atoms were successfully immobilized on V_2CT_x nanosheets using the self-reduction technique by reductive and unstable V_2CT_x .

3.3. Electrochemical performance of Pt- V_2CT_x toward HER

The HER performance of the Pt- V_2CT_x electrocatalyst was evaluated in a three-electrode system using 0.5 M H_2SO_4 and 1 M KOH electrolyte. Fig. 4a shows the HER polarization curves of V_2CT_x and Pt- V_2CT_x , together with a benchmark Pt/C (20%) electrocatalyst. The HER activity of pristine V_2CT_x was inferior with a high overpotential of 743 mV in acidic condition owing to strong O–H bonding on the surface. However, Pt- V_2CT_x , comprising Pt atoms, displayed a high current density with comparable HER performance to that of commercial Pt/C catalyst in the applied potential range. To evaluate the HER performance of Pt- V_2CT_x , we compared the potential required to reach an HER current density (j) of -10 mA cm^{-2} (a key HER performance metric) to that of the Pt/C electrocatalyst. Pt- V_2CT_x required only 27 mV vs. a reversible hydrogen electrode (RHE) overpotential to reach 10 mA cm^{-2} . In comparison, the Pt/C required the overpotential of -36.5 mV for $j = -10 \text{ mA cm}^{-2}$. Additionally, Pt- V_2CT_x required an overpotential of only -82 mV for $j = -50 \text{ mA cm}^{-2}$, enabling a fast mass-transfer process. Furthermore, Pt- V_2CT_x showed slightly enhanced kinetics in the IR-corrected HER polarization curve (Fig. S8). As shown in Fig. 4b, Pt- V_2CT_x shows a small Tafel slope of 36.5 mV dec^{-1} , revealing fast HER kinetics derived from the introduction of Pt atoms. In addition to the acidic electrolyte, Pt- V_2CT_x exhibits superior catalytic activity toward HER in basic electrolytes (1 M KOH solution) with a low overpotential of $\sim 68.1 \text{ mV}$ to reach a current density of -10 mA cm^{-2} , while the commercial Pt/C electrocatalyst requires an overpotential of $\sim 131 \text{ mV}$ (Fig. 4a). Pt- V_2CT_x exhibits a Tafel slope of 98.6 mV dec^{-1} , comparable to that of the commercial Pt/C electrocatalyst (Fig. S9). Furthermore, by normalizing to Pt content, the mass activity of HER for Pt- V_2CT_x at an overpotential of -30 mV is $7.88 \text{ A mg}_{\text{Pt}}^{-1}$, which is 50 times higher than that of the commercial Pt/C electrocatalyst (20 wt%) with $0.157 \text{ A mg}_{\text{Pt}}^{-1}$ in acidic condition. Also, Pt- V_2CT_x at an overpotential of

-50 mV displayed the mass activity of $4.02 \text{ A mg}_{\text{Pt}}^{-1}$, superior to the commercial Pt/C electrocatalyst (20 wt%) with $0.076 \text{ A mg}_{\text{Pt}}^{-1}$ in alkaline condition (Fig. 4c). Furthermore, we conducted the overall turnover frequency (TOF) calculation to employ the quantification of each active site for HER in acidic and alkaline condition (Fig. 4d). The TOF for Pt- V_2CT_x at an overpotential of 100 mV is found to be 4.74 and $1.16 \text{ H}_2 \text{ S}^{-1}$, while 20 wt% Pt/C only displayed the TOF of 0.156 and $0.0226 \text{ H}_2 \text{ S}^{-1}$ in acidic and alkaline condition, respectively. This result revealed that the introduction of atomic Pt to the V_2CT_x electrocatalyst could enhance the catalytic activity, maximizing the catalytic efficiency with a low amount of Pt loading for a highly efficient HER performance. Electrochemical impedance spectroscopy (EIS) analysis further showed that the introduction of Pt atoms into the Pt- V_2CT_x electrocatalyst results in low internal resistance and rapid charge transfer behavior at a low overpotential and fast HER kinetics (Fig. S10). The confinement of Pt at the atomic level to improve the catalytic efficiency of V_2CT_x MXene resulted in superior or comparable performance to the existing MXene-based electrocatalysts for HER (Fig. 4e) and Pt based single atom catalyst (Table S2). HER performance of Pt- V_2CT_x was compared with the reported MXene-based electrocatalysts under acidic conditions. The widely used Ti-based MXene ($Ti_3C_2T_x$) exhibits a low catalytic activity with a high overpotential exceeding 600 mV . [38] When it is modified with full O-functionalization on the surface, an overpotential of 190 mV was observed [19]. In addition, N- $Ti_3C_2T_x$ synthesized via an N doping process showed an improved HER catalytic efficiency with an overpotential of 198 mV [20]. In addition, P doping of V_2CT_x , which has a high overpotential owing to strong H–O bonds, efficiently reduced the bonding energy, demonstrating improved catalytic activity with an overpotential of 163 mV [26]. The HER catalyst prepared through complexation of Mo_2CT_x and $Ti_3C_2T_x$ with the MoS_2 layer showed efficient catalytic properties with low overpotentials of 119 and 110 mV , respectively [39,40]. However, although improved catalytic performance was achieved through various surface modifications with MXene, the overpotentials were not comparable to that of the state-of-the-art Pt/C electrocatalyst. In the case of $Mo_2TiC_2T_x$, through the bonding of atomic Pt, a very low overpotential of 30 mV was observed, indicating excellent HER performance comparable to that of a state-of-the-art

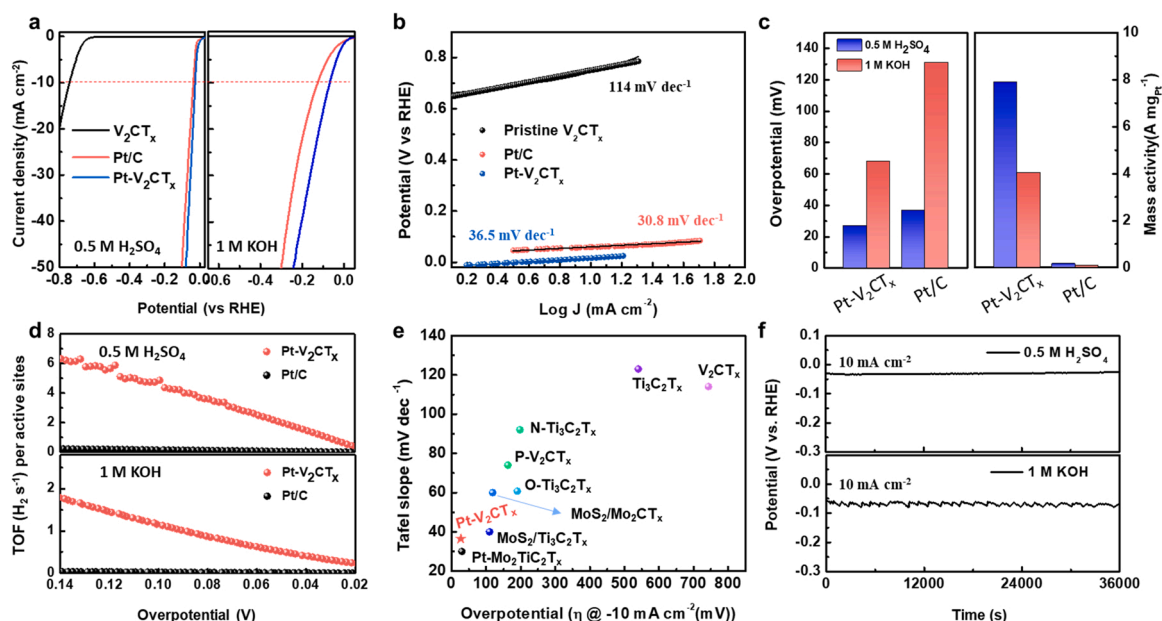


Fig. 4. Electrochemical performance for Pt- V_2CT_x and reference HER electrocatalysts. a) HER polarization curves of pristine- V_2CT_x , Pt/C (20%) and Pt- V_2CT_x , acquired using graphite rod as the counter electrode in 0.5 M H_2SO_4 solution (left) and in 1 M KOH solution (right). b) Corresponding Tafel slope derived from a. c) Comparison of overpotential (10 mA cm^{-2}) and mass activity for Pt/C (20%) and Pt- V_2CT_x catalysts in 0.5 M H_2SO_4 (blue) and 1 M KOH (red). d) Turnover frequency (TOF) of Pt/C (20%) and Pt- V_2CT_x in 0.5 M H_2SO_4 solution (top) and in 1 M KOH solution (bottom). e) Comparative graph for overpotential of related MXene based HER electrocatalysts in acidic media. f) Stability test of Pt- V_2CT_x in 0.5 M H_2SO_4 solution (top) and 1 M KOH (bottom).

electrocatalyst, Pt/C. The Pt-V₂CT_x catalyst in this study showed excellent HER catalyst performance comparable to that of the Mo-based MXene electrocatalyst [21]. These results demonstrate that V-based MXene of the same group as Mo-based materials with a d-band structure similar to Pt can achieve excellent HER performance. Furthermore, during the galvanostatic measurement conducted for 10 h to evaluate catalytic stability, Pt-V₂CT_x showed a negligible change in potential in acidic media but, in alkaline, the slight decrease of ~10 mV in overpotential (Fig. 4f). Furthermore, to study the stability and the post-characterization is highly supportive to understand the electrocatalysts. Therefore, we conducted XPS analysis and EIS analysis to study the characterizations of Pt-V₂CT_x after stability test in both 0.5 M H₂SO₄ and 1 M KOH (Fig. S11–S14). In XPS results, Pt-V₂CT_x after stability test in 0.5 M H₂SO₄ displayed the slightly oxidized state of V 2p spectrum but, there is only negligible change. However, in alkaline electrolyte test, V 2p spectra is distinctly changed indicating the higher oxidation state while the Pt 4f spectra still indicate presence of the Pt atom. As the XPS results, we confirmed that the V₂CT_x can be more easily oxidized in alkaline condition than in the acidic condition, but it can be seen that the Pt atom is stably remained. Furthermore, we conducted the EIS analysis after stability test to elucidate the electrochemical behavior of Pt-V₂CT_x both in 0.5 M H₂SO₄ and 1 M KOH. In this time, Nyquist plot also displayed the similar tendency likewise XPS results. In alkaline condition, the charge transfer resistance more increased than that in acidic condition. However, these results still displayed the low charge transfer resistance indicating the efficient HER performance. In conclusion, after stability test in alkaline condition, Pt-V₂CT_x displayed increased oxidation state than in the acidic condition. However, despite these slight changes, Pt-V₂CT_x still shows excellent catalytic performance comprising the stable immobilization of Pt atoms. These results indicate that Pt-V₂CT_x can be utilized as HER electrocatalyst with superior activity under alkaline conditions, which is required for efficient and low-cost counter electrodes (alkaline oxygen catalysts) for water splitting. Additionally, to demonstrate the catalytic contribution of Pt atoms in Pt-V₂CT_x toward HER, we conducted HER measurements with thiocyanate ions (SCN[−]). Thiocyanate ions adsorb on

the metal atoms, causing the deactivation of active metallic sites [37] Fig. S15 displays the electrocatalytic HER polarization curve of Pt-V₂CT_x with −SCN ions in 0.5 M H₂SO₄ electrolyte, indicating the overpotential of ~208 mV. The increased overpotential of Pt-V₂CT_x with −SCN proves that Pt atoms are effective active sites for HER.

3.4. DFT simulation for catalytic activity of Pt-V₂CT_x

Using DFT calculations, we demonstrated that the catalytic activity of Pt-V₂CT_x is enhanced by single Pt atoms and the V₂CT_x MXene backbone. To determine the catalytic activity of a single Pt atom on the V₂CT_x matrix, the Gibbs free energies for the adsorption of atomic hydrogen (ΔG_{H^*}) were evaluated in two different V₂CT_x systems: pristine V₂C–O₂ and strongly bound Pt at the V–O vacancy site on V₂C–O₂ (Pt–V₂C–O₂) (Fig. 5a and b). We chose the V₂C–O₂ system (Fig. 5a), a pristine V₂C surface with passivation by the terminal group (T) of O atoms adsorbed above the hollow site of C₃V₃, as studied in previous works [25,41]. The atomic hydrogen adsorbs on the O atom with ΔG_{H^*} of −0.704 eV, as per our calculations. As experimentally proved, V vacancies are naturally produced on the V₂C–O₂ surface during synthesis, and a single Pt atom can be located at the vacancy site bound to C and O atoms, as shown in Fig. 5b. During the generation of a vacancy, the V atom is detached with an adjacent O atom owing to the strong V–O bond when breaking the C–V bond, resulting in the release of V–OH₂ molecules and generating a V–O vacancy on the V₂C–O₂ surface [21]. The single Pt atom occupies this V–O vacancy site, significantly interacting with adjacent C and O atoms. The calculated binding energy of the Pt atom is −5.813 eV, which is comparable to its cohesive energy (5.84 eV/atom). The immobilized Pt single atoms at the V–O vacancies also show high catalytic activity with a ΔG_{H^*} of −0.089 eV, which is lower than that of commercial Pt catalysts (−0.10 eV). Furthermore, the catalytic activity can be enhanced over the bulk phase, as the surface area of the active sites increases with single Pt atoms confined to the V₂C–O₂ lattice.

To elucidate the catalytic contribution from immobilized Pt atoms, we investigated the density of states (DOS) of pristine V₂C–O₂ and

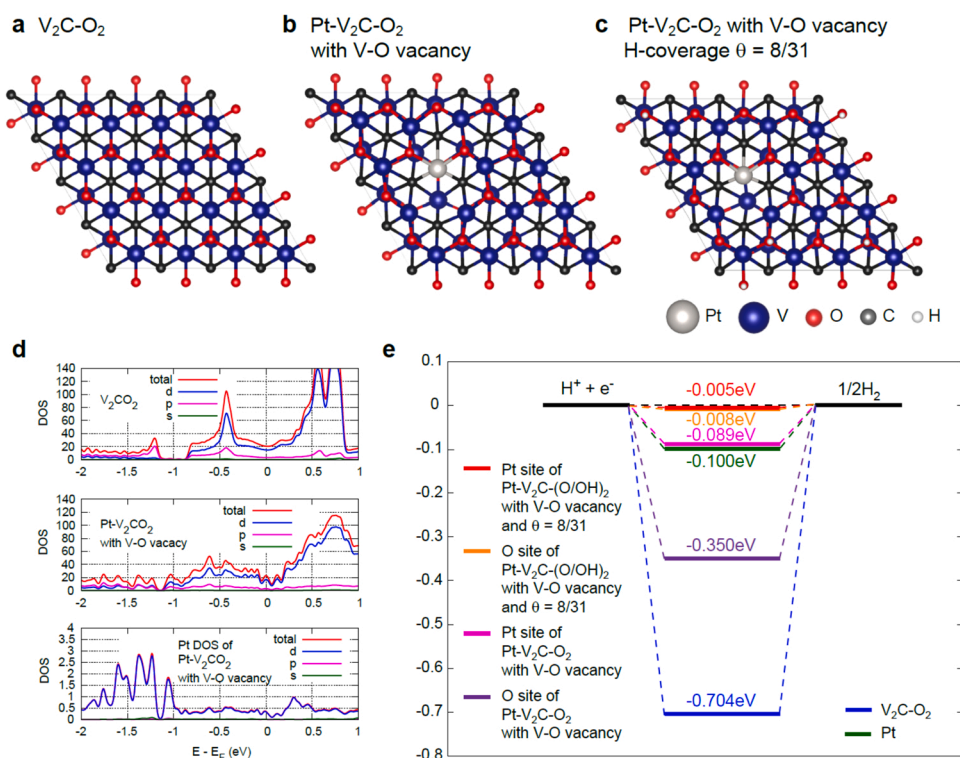


Fig. 5. DFT simulation for origin of catalytic activity. Atomic structures of (a) V₂C–O₂, (b) Pt-immobilized-V₂C–O₂ with VO vacancy, and (c) Pt-immobilized-V₂C–(O/OH)₂ with a VO vacancy and $\theta = 8/31$. The silver, blue, black, gray, and white balls represent Pt, V, O, C, and H atoms, respectively. (d) Calculated density of states (DOS) for (a) and (b) systems in order from the top. The projected DOS to s, p, d orbitals are illustrated by green, pink, blue lines. On the right hand, DOS of Pt atom is shown for (b) systems. (e) The optimal values of the Gibbs free energies for the adsorption of atomic hydrogen (ΔG_{H^*}) at Pt and O sites for (a), (b), and (c) systems.

Pt–V₂C–O₂ with V–O vacancies, as shown in Fig. 5d (top and middle panels), and the projected DOS for the *s*, *p*, and *d* atomic orbitals are depicted for each system. The projected DOS on Pt atoms in Pt–V₂C–O₂ with a V–O vacancy site is shown in the bottom panel of Fig. 5d. As demonstrated above, O and Pt atoms contribute to the HER catalytic active sites, but the V atom does not. Although the *d* electrons of V atoms dominate at the Fermi level, they are not directly involved in H adsorption. The *d* electrons of the Pt atom primarily contribute to the H adsorption. In addition, the higher occupied *d* states at the Fermi level of Pt–V₂C–O₂ with V–O vacancies than those of pristine V₂C–O₂ lead to higher conductivity and enhanced catalytic activity. A comparison of the PDOS of V₂C–O₂ and Pt–V₂C–O₂ with V–O vacancies reveals that the enhanced DOS of the latter near the Fermi level can primarily be attributed to the Pt *d* orbitals (Fig. 5d). This indicates that individual Pt atoms can effectively improve the *d*-electron domination near the Fermi level, enhancing catalytic activity.

In addition to the superior HER performance of the immobilized single Pt atoms on V₂C–O₂ with V–O vacancies, we investigated the HER catalytic activity of O terminal groups on the V₂C–O₂ backbone surface. Gao et al. suggested that the surface oxygen atoms of the pristine V₂C terminated by O/OH groups can be active sites for the HER [41]. Ling et al. proposed that the introduction of foreign transition metals on the V₂C–O₂ surface lead to the optimal free energy of hydrogen adsorption owing to electron transfer from the transition metal to O atoms [25]. In addition, the V₂C surface terminated using a mixture of O and OH functional groups is more stable than individual O or OH terminations in the acidic/alkaline solution [41]. We examined the adsorption free energy of atomic hydrogen on O atoms with different mixture ratios of O/OH terminations in our Pt–V₂C–O₂ system (Fig. S16 and 17). In the 4 × 4 × 1 supercell structure, a single Pt atom is located at a V–O vacancy site, and 31 O atoms act as the available adsorption sites of atomic hydrogen, some of which are changed to OH termination, denoted by the H-coverage θ . For $\theta = 0$ (implying all V atoms are passivated by O atoms rather than OH terminations), the average value of the Gibbs free energy of hydrogen adsorption on 31 O atoms was –0.531 eV, and the optimal ΔG_{H^+} was –0.350 eV. The ΔG_{H^+} values were enhanced compared to ΔG_{H^+} of pristine V₂C–O₂ (–0.704 eV). Electrons transfer from Pt to O atoms, leading to an improved electron environment for catalyzing the HER of oxygen sites. [25].

For $\theta = 8/31$, where 31 V atoms are passivated by 8 OH and 23 O atoms (Fig. S16), the average value of ΔG_{H^+} is –0.157 eV for approximately 23 O atoms; among them, eight O sites have an absolute value of free energy $|\Delta G_{H^+}|$ less than 0.1 eV, which is optimal for HER catalytic activity. The optimal value of ΔG_{H^+} on the O atom was –0.008 eV. (Fig. 5e) The positions of the eight OH terminations were chosen in the order of the strongest hydrogen adsorption sites at $\theta = 0$. The mixture of O and OH terminations further enhances the HER performance of O atoms along with the single Pt atoms. For comparison, we evaluated ΔG_{H^+} at the H-coverage of $\theta = 8/32$ on pristine V₂C–O₂, and the average ΔG_{H^+} was also enhanced to 0.096 eV. This improvement in the catalytic activity of O atoms is associated with the H-coverage rather than Pt atoms. From the Bader charge analysis (Table S3, Supporting Information), the average number of electrons from O atoms increases by 0.036e and 0.235e per active O atom and H-covered O atom, respectively, compared to the O atoms when $\theta = 0$ in the Pt–V₂C–O₂ system with V–O vacancies. For the pristine V₂C–O₂ system, the increase in the number of electrons of the O atoms is 0.029e and 0.226e for the active O atoms and H-covered O atoms, respectively. Bader charge analysis revealed that electrons are transferred from OH functional groups to O atoms. Because of excess electrons, when the H atom is adsorbed on the active O atom, the electrons fill the anti-bonding orbital σ^* of the O–H bonds and weaken them [25]. In addition to the active O atoms, electron transfer from the OH termination enhances ΔG_{H^+} of the Pt atom to –0.005 eV with increased conductivity of the backbone structure, as illustrated in Fig. 5e. For an H-coverage of 16/31, the average value of ΔG_{H^+} is 0.252 eV for approximately 15 O atoms, and the interaction

strength becomes weaker than $\theta = 0$ and 8/31. Excess electrons residing on O atoms (an increase by 0.072e per active O atom) lead to considerable weakening of the O–H bonds. These results indicate that the optimal H-coverage of $\theta = 8/31$ leads to improved HER catalytic activity with a single Pt atom.

4. Conclusion

In conclusion, atomic Pt immobilization into V-based MXene nanosheets was achieved via a self-reduction process of Pt by the highly reductive nature of V₂CT_x to accelerate HER. The vacancy sites naturally generated during synthesis of V₂CT_x nanosheets acted as reductive sites for the immobilization of Pt atoms. Atomically introduced Pt atoms enhanced the electrocatalytic efficiency and promoted electron transfer of additional active sites to the surrounding atoms to activate the V₂CT_x nanosheets. DFT calculations suggested that the atomic Pt atoms confined to the V vacancies act as efficient active sites and reduce the H–O binding energy by charge transfer from the Pt atom to the surrounding atoms, resulting in the optimal adsorption energy and outstanding HER performance.

CRediT authorship contribution statement

Seungyoung Park: Conceptualization, Writing – original draft, Writing – review & editing, Formal analysis, Investigation, Data curation, Formal analysis, Validation, Visualization. **Yea-Lee Lee:** Writing – original draft, DFT simulation, Validation, Visualization. **Yeoheung Yoon:** Methodology, Validation. **Se Yeon Park:** Investigation. **Soonmin Yim:** Validation, Visualization. **Woosook Song:** Validation, Visualization. **Sung Myung:** Validation, Visualization. **Kug-Seung Lee:** XAS experiment & analysis. **Hyunju Chang:** DFT simulation. **Sun Sook Lee:** Writing – review & editing, Supervision. **Ki-Seok An:** Supervision.

Declaration of Competing Interest

The authors declare that they have no known competing financial interests or personal relationships that could have appeared to influence the work reported in this paper.

Acknowledgements

S. P., Y.-L. L. contributed equally to this work. This research was supported by Development of smart chemical materials for IoT device Project through the Korea Research Institute of Chemical Technology (KRICT) of Republic of Korea. (SS2121-10). This research was supported by the Nano/Material Technology Development Program through the National Research Foundation of Korea (NRF) funded by the Ministry of Education, Science and Technology (NRF-2017M3D9A1073502). The computational work was supported by the National Supercomputing Center with supercomputing resources including technical support (KSC-2021-CRE-0144). This work was supported by the National Research Foundation of Korea (NRF) grant funded by the Korea government (MSIP) (NRF-2018M1A2A2061998).

Appendix A. Supporting information

Supplementary data associated with this article can be found in the online version at doi:10.1016/j.apcatb.2021.120989.

References

- [1] W. Lubitz, W. Tumas, Hydrogen: an Overview, Chem. Rev. 107 (2007) 3900–3903, <https://doi.org/10.1021/cr050200z>.
- [2] C.G. Morales-Guio, L.-A. Stern, X. Hu, Nanostructured hydrotreating catalysts for electrochemical hydrogen evolution, Chem. Soc. Rev. 43 (2014) 6555, <https://doi.org/10.1039/c3cs60468c>.

- [3] M.S. Faber, S. Jin, Earth-abundant inorganic electrocatalysts and their nanostructures for energy conversion applications, *Energy Environ. Sci.* 7 (2014) 3519–3542, <https://doi.org/10.1039/c4ee01760a>.
- [4] X. Zou, Y. Zhang, Noble metal-free hydrogen evolution catalysts for water splitting, *Chem. Soc. Rev.* 44 (2015) 5148–5180, <https://doi.org/10.1039/c4cs00448e>.
- [5] I. Roger, M.A. Shipman, M.D. Symes, Earth-abundant catalysts for electrochemical and photoelectrochemical water splitting, *Nat. Rev. Chem.* 1 (2017), <https://doi.org/10.1038/s41570-016-0003>.
- [6] J. Yang, Y. Wang, M.J. Lagos, V. Manichev, R. Fullon, X. Song, D. Voiry, S. Chakraborty, W. Zhang, P.E. Batson, L. Feldman, T. Gustafsson, M. Chhowalla, Single atomic vacancy catalysis, *ACS Nano* 13 (2019) 9958–9964, <https://doi.org/10.1021/acsnano.9b05226>.
- [7] Y. Shi, B. Zhang, Recent advances in transition metal phosphide nanomaterials: synthesis and applications in hydrogen evolution reaction, *Chem. Soc. Rev.* 45 (2016) 1529–1541, <https://doi.org/10.1039/c5cs00434a>.
- [8] Y. Zhong, X. Xia, F. Shi, J. Zhan, J. Tu, H.J. Fan, Transition metal carbides and nitrides in energy storage and conversion, *Adv. Sci.* 3 (2016), 1500286, <https://doi.org/10.1002/advs.201500286>.
- [9] Z. Chen, X. Duan, W. Wei, S. Wang, B.-J. Ni, Recent advances in transition metal-based electrocatalysts for alkaline hydrogen evolution, *J. Mater. Chem. A* 7 (2019) 14971–15005, <https://doi.org/10.1039/c9ta03220g>.
- [10] X. Yu, Z.-Y. Yu, X.-L. Zhang, Y.-R. Zheng, Y. Duan, Q. Gao, R. Wu, B. Sun, M.-R. Gao, G. Wang, S.-H. Yu, “Superaerophobic” nickel phosphide nanoarray catalyst for efficient hydrogen evolution at ultrahigh current densities, *J. Am. Chem. Soc.* 141 (2019) 7537–7543, <https://doi.org/10.1021/jacs.9b02527>.
- [11] D.W. Su, J. Ran, Z.W. Zhuang, C. Chen, S.Z. Qiao, Y.D. Li, G.X. Wang, Atomically dispersed Ni in cadmium-zinc sulfide quantum dots for high-performance visible-light photocatalytic hydrogen production, *Sci. Adv.* 6 (2020), eaz8447 doi: 10.1126/sciadv.aaz8447.
- [12] L. Wu, A. Longo, N.Y. Dzade, A. Sharma, M.M.R.M. Hendrix, A.A. Bol, N.H. Leeuw, E.J.M. Hensen, J.P. Hofmann, The origin of high activity of amorphous MoS₂ in the hydrogen evolution reaction, *ChemSusChem* 12 (2019) 4383–4389, <https://doi.org/10.1002/cssc.201901811>.
- [13] M. Ghidui, M.R. Lukatskaya, M.-Q. Zhao, Y. Gogotsi, M.W. Barsoum, Conductive two-dimensional titanium carbide ‘clay’ with high volumetric capacitance, *Nature* 516 (2014) 78–81, <https://doi.org/10.1038/nature13970>.
- [14] Y. Gogotsi, B. Anasori, The rise of MXenes, *ACS Nano* 13 (2019) 8491–8494, <https://doi.org/10.1021/acsnano.9b06394>.
- [15] K. Montazeri, M. Currie, L. Verger, P. Dianat, M.W. Barsoum, B. Nabet, Beyond gold: spin-coated Ti₃C₂-based mxene photodetectors, *Adv. Mater.* 31 (2019), 1903271, <https://doi.org/10.1002/adma.201903271>.
- [16] V. Shukla, The tunable electric and magnetic properties of 2D MXenes and their potential applications, *Mater. Adv.* 1 (2020) 3104–3121, <https://doi.org/10.1039/d0ma00548g>.
- [17] B. Anasori, M.R. Lukatskaya, Y. Gogotsi, 2D metal carbides and nitrides (MXenes) for energy storage, *Nat. Rev. Mater.* 2 (2017), <https://doi.org/10.1038/natrevmats.2016.98>.
- [18] Z.W. Seh, K.D. Fredrickson, B. Anasori, J. Kibsgaard, A.L. Strickler, M. R. Lukatskaya, Y. Gogotsi, T.F. Jaramillo, A. Vojvodic, Two-Dimensional Molybdenum Carbide (MXene) as an Efficient Electrocatalyst for Hydrogen, *Evol., ACS Energy Lett.* 1 (2016) 589–594, <https://doi.org/10.1021/acscenergylett.6b00247>.
- [19] T.A. Le, Q.V. Bui, N.Q. Tran, Y. Cho, Y. Hong, Y. Kawazoe, H. Lee, Synergistic effects of nitrogen doping on MXene for enhancement of hydrogen evolution reaction, *ACS Sustain. Chem. Eng.* 7 (2019) 16879–16888, <https://doi.org/10.1021/acssuschemeng.9b04470>.
- [20] Y. Jiang, T. Sun, X. Xie, W. Jiang, J. Li, B. Tian, C. Su, Oxygen-functionalized ultrathin Ti₃C₂T_x MXene for enhanced electrocatalytic hydrogen evolution, *ChemSusChem* 12 (2019) 1368–1373, <https://doi.org/10.1002/cssc.201803032>.
- [21] J. Zhang, Y. Zhao, X. Guo, C. Chen, C.-L. Dong, R.-S. Liu, C.-P. Han, Y. Li, Y. Gogotsi, G. Wang, Single platinum atoms immobilized on an MXene as an efficient catalyst for the hydrogen evolution reaction, *Nat. Catal.* 1 (2018) 985–992, <https://doi.org/10.1038/s41929-018-0195-1>.
- [22] J.M. Gonçalves, M. Ireno da Silva, L. Angnes, K. Araki, Vanadium-containing electro and photocatalysts for the oxygen evolution reaction: a review, *J. Mater. Chem. A* 8 (2020) 2171–2206, <https://doi.org/10.1039/c9ta10857b>.
- [23] M.D. Dolan, M.E. Kellam, K.G. McLennan, D. Liang, G. Song, Hydrogen transport properties of several vanadium-based binary alloys, *Int. J. Hydrog. Energy* 38 (2013) 9794–9799, <https://doi.org/10.1016/j.ijhydene.2013.05.073>.
- [24] J.M. Gonçalves, P.R. Martins, K. Araki, L. Angnes, Recent progress in water splitting and hybrid supercapacitors based on nickel-vanadium layered double hydroxides, *J. Energ. Chem.* 57 (2021) 496–515, <https://doi.org/10.1016/j.jechem.2020.08.047>.
- [25] C. Ling, L. Shi, Y. Ouyang, Q. Chen, J. Wang, Transition metal-promoted V₂CO₂ (MXenes): a new and highly active catalyst for hydrogen evolution reaction, *Adv. Sci.* 3 (2016), 1600180, <https://doi.org/10.1002/advs.201600180>.
- [26] Y. Yoon, A.P. Tiwari, M. Choi, T.G. Novak, W. Song, H. Chang, T. Zyung, S.S. Lee, S. Jeon, K. An, Precious-metal-free electrocatalysts for activation of hydrogen evolution with nonmetallic electron donor: chemical composition controllable phosphorous doped vanadium carbide MXene, *Adv. Funct. Mater.* 29 (2019), 1903443, <https://doi.org/10.1002/adfm.201903443>.
- [27] K. Jiang, B. Liu, M. Luo, S. Ning, M. Peng, Y. Zhao, Y.-R. Lu, T.-S. Chan, F.M.F. de Groot, Y. Tan, Single platinum atoms embedded in nanoporous cobalt selenide as electrocatalyst for accelerating hydrogen evolution reaction, *Nat. Commun.* 10 (2019), <https://doi.org/10.1038/s41467-019-09765-y>.
- [28] D. Li, X. Chen, Y. Lv, G. Zhang, Y. Huang, W. Liu, Y. Li, R. Chen, C. Nuckolls, H. Ni, An effective hybrid electrocatalyst for the alkaline HER: Highly dispersed Pt sites immobilized by a functionalized NiRu-hydroxide, *Appl. Catal. B: Environ.* 269 (2020), 118824, <https://doi.org/10.1016/j.apcatb.2020.118824>.
- [29] P. Kuang, Y. Wang, B. Zhu, F. Xia, C. Tung, J. Wu, H.M. Chen, J. Yu, Pt single atoms supported on N-doped mesoporous hollow carbon spheres with enhanced electrocatalytic H₂-evolution activity, *Adv. Mater.* 33 (2021), 2008599, <https://doi.org/10.1002/adma.202008599>.
- [30] G. Kresse, J. Furthmüller, Efficiency of ab-initio total energy calculations for metals and semiconductors using a plane-wave basis set, *Comp. Mater. Sci.* 6 (1996) 15–50, [https://doi.org/10.1016/0927-0256\(96\)00008-0](https://doi.org/10.1016/0927-0256(96)00008-0).
- [31] G. Kresse, J. Furthmüller, Efficient iterative schemes for ab initio total-energy calculations using a plane-wave basis set, *Phys. Rev. B* 54 (1996) 11169–11186, <https://doi.org/10.1103/physrevb.54.11169>.
- [32] A. Tkatchenko, M. Scheffler, Accurate molecular Van Der Waals interactions from ground-state electron density and free-atom reference data, *Phys. Rev. Lett.* 102 (2009), <https://doi.org/10.1103/physrevlett.102.073005>.
- [33] D. Zhao, Z. Chen, W. Yang, S. Liu, X. Zhang, Y. Yu, W.-C. Cheong, L. Zheng, F. Ren, G. Ying, X. Cao, D. Wang, Q. Peng, G. Wang, C. Chen, MXene (Ti₃C₂) vacancy-confined single-atom catalyst for efficient functionalization of CO₂, *J. Am. Chem. Soc.* 141 (2019) 4086–4093, <https://doi.org/10.1021/jacs.8b13579>.
- [34] M. Naguib, J. Halim, J. Lu, K.M. Cook, L. Hultman, Y. Gogotsi, M.W. Barsoum, New two-dimensional niobium and vanadium carbides as promising materials for Li-Ion batteries, *J. Am. Chem. Soc.* 135 (2013) 15966–15969, <https://doi.org/10.1021/ja405735d>.
- [35] Y. Tang, Q. Liu, L. Dong, H.B. Wu, X.-Y. Yu, Activating the hydrogen evolution and overall water splitting performance of NiFe LDH by cation doping and plasma reduction, *Appl. Catal. B Environ.* 266 (2020), 118627, <https://doi.org/10.1016/j.apcatb.2020.118627>.
- [36] M. Naguib, R.R. Unocic, B.L. Armstrong, J. Nanda, Large-scale delamination of multi-layers transition metal carbides and carbonitrides MXenes, *Dalton Trans.* 44 (2015) 9353–9358, <https://doi.org/10.1039/c5dt01247c>.
- [37] H. Zhang, P. An, W. Zhou, B.Y. Guan, P. Zhang, J. Dong, X.W. (David) Lou, Dynamic traction of lattice-confined platinum atoms into mesoporous carbon matrix for hydrogen evolution reaction, *Sci. Adv.* 4 (2018) ea06657, <https://doi.org/10.1126/sciadv.aao6657>.
- [38] S. Li, P. Tuo, J. Xie, X. Zhang, J. Xu, J. Bao, B. Pan, Y. Xie, Ultrathin MXene nanosheets with rich fluorine termination groups realizing efficient electrocatalytic hydrogen evolution, *Nano Energy* 47 (2018) 512–518, <https://doi.org/10.1016/j.nanoen.2018.03.022>.
- [39] K.R.G. Lim, A.D. Handoko, L.R. Johnson, X. Meng, M. Lin, G.S. Subramanian, B. Anasori, Y. Gogotsi, A. Vojvodic, Z.W. Seh, 2H-MoS₂ on Mo₂CT_x MXene nanohybrid for efficient and durable electrocatalytic hydrogen evolution, *ACS Nano* 14 (2020) 16140–16155, <https://doi.org/10.1021/acsnano.0c08671>.
- [40] N.H. Attanayake, S.C. Abeyweera, A.C. Thenuwara, B. Anasori, Y. Gogotsi, Y. Sun, D.R. Strongin, Vertically aligned MoS₂ on Ti₃C₂ (MXene) as an improved HER catalyst, *J. Mater. Chem. A* 6 (2018) 16882–16889, <https://doi.org/10.1039/c8ta05033c>.
- [41] G. Gao, A.P. O’Mullane, A. Du, 2D MXenes: a new family of promising catalysts for the hydrogen evolution reaction, *ACS Catal.* 7 (2016) 494–500, <https://doi.org/10.1021/acscatal.6b02754>.